ACS SENSORS

Compact Differential Photoacoustic Exhaled Gas Sensor for Online $ETCO_2$ and ETO_2 Monitoring

Xukun Yin, Chenchen Zhu, Xiu Yang, Lei Liu, Dacheng Zhang, Kaijie Xu, Hongzhi Wang,
Shuangping Zhang,* Nicoletta Ardito, Pietro Patimisco, Angelo Sampaolo, Vincenzo Spagnolo,*
Hongpeng Wu,* and Huailiang Xu*

Cite This: https://doi.org/10.1021/acssensors.5c03835 Read Online

ACCESS | Metrics & More | Article Recommendations | Supporting Information

ABSTRACT: Online exhaled breath analysis holds great promise for noninvasive medical diagnostics, health monitoring, and environmental exposure assessment. However, the complex nature of the breath matrix and strong interference from water vapor and carbon dioxide make high-precision, real-time sensing challenging, often requiring large and costly systems such as mass spectrometers. In this work, we present a compact differential photoacoustic gas sensor for end-tidal carbon dioxide ($ETCO_2$) and end-tidal oxygen (ETO_2) monitoring. The sensor employs a dual-resonator photoacoustic cell with resonant frequencies of 4110 and 13,115 Hz for selective $ETCO_2$ and ETO_2 detection, respectively. A small sample gas volume of 2.6 mL enables a rapid response time of <0.5 s, enabling rapid tracking of changes in exhaled gas concentration. The optimized system achieves detection limits of 12.6 ppm for CO_2 and 18.4 ppm for O_2, with corresponding normalized noise equivalent absorption values of 2.9×10^{-8} and 1.6×10^{-7} $cm^{-1} \cdot W \cdot Hz^{-1/2}$. Real-time monitoring during human respiration demonstrates clear tracking of physiological O_2 depletion and CO_2 enrichment, consistent with respiratory dynamics. The developed sensor combines high sensitivity, fast response, compact size, and low cost, showing strong potential for continuous clinical monitoring, perioperative care, and metabolic studies.

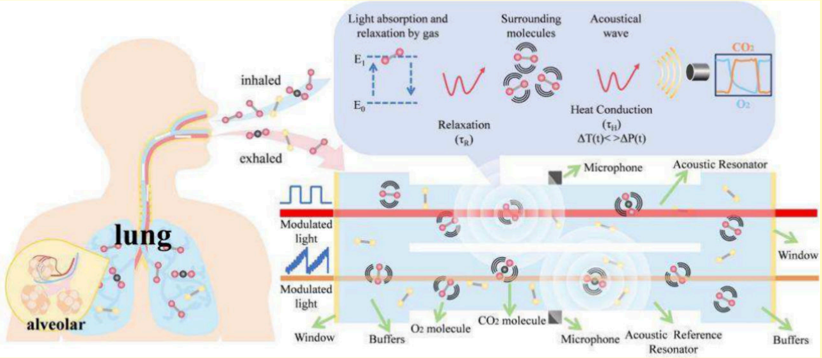

KEYWORDS: *photoacoustic spectroscopy, trace gas sensors, exhaled breath, end-tidal oxygen monitoring, red diode laser*

Online exhaled breath analysis is rapidly emerging as a powerful approach for medical diagnosis and personalized healthcare. It provides noninvasive, real-time insight into a patient's metabolic status by detecting a wide range of endogenous and exogenous compounds. With virtually unlimited sample availability, it enables continuous monitoring of health status, disease progression, and therapeutic response. This technique is particularly valuable in emergencies and critical care settings where immediate results are essential, such as the management of pneumonia, detection of drugs, and anti-doping testing.[1,2] The noninvasive profiling of airway and systemic biomarkers has thus become a key research focus, offering a unique window into respiratory physiology and metabolic processes. For this purpose, the end-tidal phase of exhalation is generally considered as the most reliable sampling stage, as it provides a stable flow and maximal concentrations of alveolar gases. The process of breathing can be compared to flushing a long pipeline. During the early phase of exhalation, the exhaled gas originates from the trachea and bronchi, which constitute the anatomical dead space. This portion of gas does not participate in alveolar gas exchange and is therefore primarily inhaled air, with a composition similar to ambient air, providing limited physiological information. In the mid-exhalation phase, a mixture of dead space gas and alveolar gas is exhaled. During the end-exhalation phase, instead, the final exhaled air almost entirely originates from the alveoli, the primary sites of gas exchange, where volatile compounds in the blood diffuse into the alveolar gas.[3−7] Thus, the composition of this final portion of breath closely reflects blood concentration and body metabolic state. Monitoring end-tidal carbon dioxide ($ETCO_2$) and end-tidal oxygen (ETO_2)

Received: October 15, 2025
Revised: December 18, 2025
Accepted: January 15, 2026

is a critical component of modern healthcare, providing essential information for maintaining patient safety.[8−11] When measured simultaneously, these parameters offer clinicians a comprehensive, real-time assessment of a patient's respiratory, circulatory, and metabolic status, thereby enhancing safety during anesthesia, surgery, and critical care. Breath analysis progressed from ancient empirical observations to a sophisticated, interdisciplinary field of research. Early references can be traced to traditional Chinese medicine and Hippocratic teachings, which associated characteristic breath odors with specific diseases, for instance, a sweet scent with diabetes and a putrid odor with pulmonary abscess. A major milestone occurred in 1971, when Linus Pauling applied gas chromatography to identify more than 250 volatile organic compounds (VOCs) in frozen breath samples, establishing the foundation for modern breathomics.[12] Since then, several breath-based diagnostic tests have been standardized and incorporated into clinical practice, including ethanol breath testing, fractional exhaled nitric oxide (FeNO) for asthma monitoring, hydrogen (H_2) and methane (CH_4) tests for small intestinal bacterial overgrowth, and the ^{13}C-urea breath test for Helicobacter pylori infection. Currently, gas chromatography mass spectrometry (GC-MS) remains the most widely used analytical platform for breath research owing to its high selectivity and robust compound identification capabilities. The advent of real-time mass spectrometric techniques, including selected ion flow tube mass spectrometry, proton transfer reaction mass spectrometry, and secondary electrospray ionization mass spectrometry, has enabled online monitoring of VOCs with exceptional temporal resolution. When coupled with high-resolution mass analyzers, these soft ionization methods have substantially expanded metabolite coverage and facilitated untargeted compound discovery.[13−15] However, the inherent need for sample preparation introduces several limitations, including sample degradation, adsorption losses, and potential contamination. Additionally, the offline nature of GC-MS leads to delayed analysis and limited temporal resolution. Furthermore, the high relative humidity and body-temperature conditions (approximately 37 °C) of exhaled breath complicate direct MS analysis, restricting the comparability and reproducibility of results.

Portable breath analyzers based on chemical sensors offer potential for point-of-care detection of ammonia,[16] acetone,[17] formaldehyde,[18] and even aldehyde detection;[19] however, they are presently constrained by limited multianalyte detection capability and susceptibility to interference arising from the complex composition of exhaled breath. Recently, optical gas sensors have gained increasing attention due to their high detection accuracy and minimal cross-interference, making them particularly suitable for breath analysis. To enhance detection sensitivity, multipass optical absorption cells are commonly employed. For instance, tunable diode laser absorption spectroscopy technology employs a white cell or a Herriott cell, providing optical path lengths ranging from approximately 0.1 to 80 m, thereby amplifying absorbance in accordance with the Lambert–Beer law.[20−22] Furthermore, optical-cavity-based techniques, including cavity ring-down spectroscopy, integrated cavity output spectroscopy, and cavity-enhanced absorption spectroscopy, achieve effective optical path lengths on the order of several kilometers, substantially improving trace gas detection sensitivity.[23,24] However, the use of large-volume cells introduces certain drawbacks: it increases the sensor's response time, amplifies susceptibility to environmental fluctuations, and limits the detection of high-concentration gases due to photodetector performance constraints.

Photoacoustic spectroscopy (PAS) is an indirect optical absorption technique particularly suitable for exhaled breath sensing, as it detects acoustic waves generated by modulated light absorption rather than light intensity.[25−29] The main advantage of PAS is its ability to operate with different laser types and wavelengths, making it well-suited for the detection of various gases and adaptable for multigas sensing configurations. Another unique advantage of PAS is that the sensing limit is proportional to the excitation power within the linear absorption regime, until saturation effects occur at higher powers. [30−34] To achieve high detection sensitivity, it is essential to select strong absorption lines and employ sufficient excitation power.

Simultaneous measurement of multiple gases has become increasingly important in various applications, including medical diagnostics, environmental monitoring, industrial process control, and safety surveillance. Multigas detection provides real-time monitoring of complex gas mixtures, improves detection efficiency, and delivers more comprehensive information than single-gas measurements, which is critical for understanding physiological processes, pollution sources, and chemical reactions. Several advanced optical spectroscopy techniques have been developed for multigas detection, including QCL-based dual-spectroscopy,[35] self-calibrated $2f/1f$ wavelength modulation spectroscopy,[36] quartz tuning fork enhanced laser spectroscopy,[37] and spherical photoacoustic cell enhanced PAS.[38] These techniques have successfully demonstrated simultaneous detection of three or more gases, providing important references and guidance for practical applications and the development of versatile gas sensors.[39−41]

In this work, a low-cost red diode laser is employed as the excitation source for online ETO_2 detection. Its high output power of approximately 3 W ensures excellent O_2 detection accuracy. Additionally, a near-infrared distributed feedback laser (DFB) with an output wavelength of 2004 nm is simultaneously employed for $ETCO_2$ detection. The system utilized a compact two-resonator photoacoustic cell with a small sample gas volume of only 2.6 mL, resulting in a response time below 0.5 s. This configuration enables the sensor to rapidly track variations in exhaled gas concentrations.

■ ABSORPTION LINE SELECTION

Most of laser-spectroscopy-based O_2 gas sensors use the O_2 molecule's A-band ($b^1\Sigma_g^+ \leftarrow X^3\Sigma_g^-$) absorption band near the wavenumber of 13,100 cm^{-1} as the excitation source, which is the strongest band in the visible and infrared range. However, the optical transition of the A-band is dipole forbidden, with vibrational and rotational structures, leading to a comparatively low spectral absorption of $\sim 8.5 \times 10^{-24}$ cm/molecule. The transition is nevertheless optically active because the triplet ground state has a permanent magnetic dipole moment. As shown in Figure S1a, a red diode laser with a central wavelength of 764.89 nm was selected, providing a high output power of ~3 W. Besides, as shown in Figure S1b, a near-infrared DFB laser emitting at 2004.02 nm was used, corresponding to a CO_2 spectral absorption intensity of $\sim 1.32 \times 10^{-21}$ cm/molecule for $ETCO_2$ detection. As shown in Figure S2, despite the mid-infrared spectral line is over 100 times larger than the selected line, the high cost of the required laser and driver system makes this approach unsuitable for real-time CO_2 detection. Although 1572−1580 nm DFB lasers are more cost-effective, the strongest absorption lines in this region are nearly two orders of magnitude weaker than those near 2004.02 nm according to the HITRAN database. Considering both absorption strength and the recent reduction in the cost of 2004.02 nm lasers, which are now only about twice as expensive as typical 1572 nm devices, the 2004.02 nm line provides a better balance between sensitivity and system performance for breath CO_2 measurement. Using the developed differential photoacoustic cell, the achieved detection limit is adequate for breath CO_2 analysis. In addition, 400 ppm CO_2 and 2% H_2O absorption curves are depicted in Figure S3, demonstrating interference-free $ETCO_2$ measurement in breath.[42]

PHOTOACOUSTIC CELL SIMULATION AND DESIGN

To carry out the CO_2 and O_2 gas detection simultaneously, a photoacoustic cell with two identical resonators was first simulated. Further information on the photoacoustic cell is supplied in the supplementary material. As a result, the photoacoustic signal S is proportional to the cell constant C_{cell}, excitation laser power P, gas concentration C, and gas absorption coefficient α, i.e., $S = C_{cell}PC\alpha$.[43−45] To carry out simultaneous high-precision measurements of $ETCO_2$ and ETO_2, a two-resonator photoacoustic cell was designed. Each resonant cavity is 35 mm in length with an internal diameter of 4 mm. Two microphones are mounted at the antinode position of the cavity. Moreover, two buffer chambers are placed at both ends of the resonators to reduce the gas-flow-induced noise; each chamber is 8 mm long and has an internal diameter of 12 mm. The inner volume of the developed photoacoustic cell is just 2.6 mL, although it employs two resonators and buffer chambers, which ensures a faster gas response than the conventional photoacoustic cells.[46−49] To further evaluate the performance of the photoacoustic cell, COMSOL software was used to simulate the frequency and photoacoustic signal. For the simulation, standard air has been selected as a fluid medium inside the photoacoustic cell cavity. At a temperature of 293.14 K and a pressure of 1 atm, its density is 1.204 kg/m^3, and the speed of sound is 343.23 m/s. A refined physics-based mesh is used to discretize the 3D model of the photoacoustic cell. COMSOL was employed to scan the cell over a frequency range of 2000−15,000 Hz with a step size of 1 Hz. As shown in Figure 1, four resonant frequencies in longitudinal mode of $F_1 = 4110$ Hz, $F_2 = 4761$ Hz, $F_3 =12{,}539$ Hz, and $F_4 = 13{,}115$ Hz are calculated for each resonant cavity between 2000 and 150,00 Hz. From the color illustration of Figure 1a, the sound pressure is depicted for different frequencies. In the simulation cloud map, the color of the sound pressure ranges from blue to red, indicating that the sound pressure increases. The areas with colors close to dark blue have the lowest sound pressure, and green represents a sound pressure of 0. It should be noted that the middlemost signal phases of F_1 and F_4 are negative in the two resonators. However, the phase valves are positive for F_2 and F_3. By using a homemade differential circuit, only the F_1 and F_4 signals can be retained for gas sensing. The peak values of the sound pressure signals differ by ∼3 times.

In addition, a very weak signal appears near 9600 Hz in the simulation results. This signal originates from a longitudinal acoustic mode of the resonator, although the maximum acoustic pressure of this mode does not occur at the center of the cavity where the microphones are located. A small residual acoustic pressure is still present at the center, which leads to the weak signal observed in Figure 1. Because its amplitude is nearly two orders of magnitude lower than that of the F_1 mode and cannot provide usable sensitivity, this mode is not considered in the gas sensing measurements.

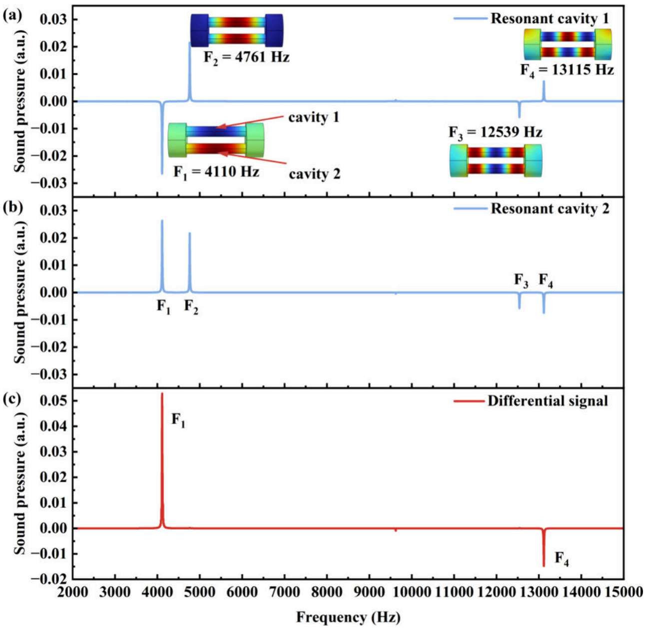

Figure 1. Photoacoustic sound pressure simulation of resonant cavity 1 (a) and cavity 2 (b). The sound pressure cloud maps of four different frequencies are inserted in panel (a). After the differential calculation, the sound pressure of two resonant frequencies is depicted in panel (c).

In order to verify the simulation results, the photoacoustic cell resonant frequency is experimentally scanned between 2000 and 15,000 Hz. The scan step is 1 Hz. As shown in Figure S4, two strong frequency curves with the center frequencies of 4001.6 and 10689.8 Hz are achieved and correspond to the F_1 and F_4 modes. The measured full widths at half-maximum are 621 and 375 Hz, respectively. According to eq S7, the Q-factor results are 6.5 and 28.5, respectively. For the following experiment, the F_1 frequency representing the photoacoustic cell will be used for ETO_2 sensing, while the F_4 frequency will be employed for $ETCO_2$ sensing.

EXPERIMENTAL PROCEDURE AND SETUP

To enable simultaneous online detection of two gases, a laboratory-based indoor differential PAS sensing system was developed, as illustrated in Figure 2. A red diode laser (MDL-XF-760, Changchun New Industries Optoelectronics Tech) with a central wavelength of 764.9 nm was modulated at 4001 Hz for O_2 sensing using 1*f* intensity-modulation detection since the laser wavelength was not tunable. The optimization results of the laser duty ratio from 30 to 70% are shown in Figure S5. The maximum photoacoustic signal of 4.3 mV was obtained at a 50% duty ratio under a 20% O_2 standard gas mixture. After passing through the photoacoustic cell (PAC), the laser output power was measured with a power meter (3A, Ophir Optronics Solutions) and found to be 1.328 W at a 50% duty cycle. For CO_2 detection, a 2004 nm butterfly DFB laser (EP2004-0-DM-B06-FM, Eblana Photonics) was modulated with a slow-scan saw-tooth wave and a fast-scan sine wave. The output power measured after the PAC was 2.35 mW. The sine-wave modulation frequency was set to half of the F_4 mode (5344.9 Hz) to implement the 2*f* wavelength modulation detection. Two uncoated CaF_2 windows (WG51050, Thorlabs) with a diameter of 25.4 mm and a thickness of 5 mm were mounted at both ends of the PAC to minimize optical absorption losses for the visible and near-infrared laser sources. Two low-noise electret condenser

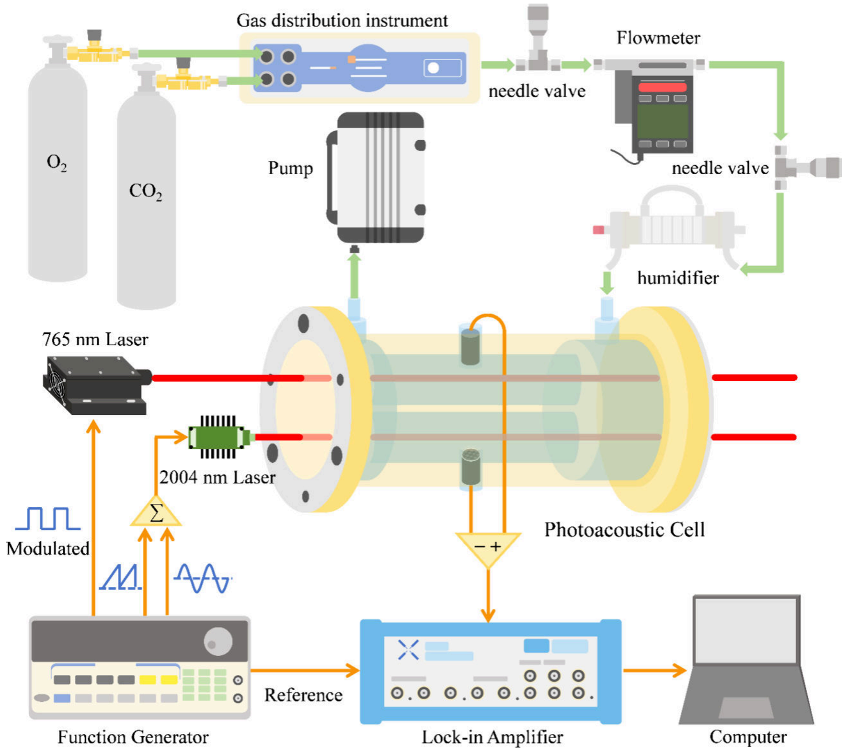

Figure 2. Schematic of the photoacoustic gas sensor system for $ETCO_2$ and ETO_2 detection.

microphones (EM258, Primo Microphones Inc., sensitivity −32 ± 3 dB) were placed at the longitudinal centers of the two differential channels to collect the standing waves in the designed differential PAC. After a differential circuit and a preamplifier, the signal was fed into a dual-channel lock-in amplifier (MFLI, Zurich Instruments). The lock-in parameters were set to a 12 dB/oct filter slope and a 1 s time constant, corresponding to a detection bandwidth of 0.25 Hz. A computer was used to acquire and process the signals via a Labview program from both the lock-in amplifier and the power meter. A gas dilution system (GB 103, MCQ), a diaphragm pump (N813.5ANE, KNF), and a needle valve were used to control and maintain the gas flow and pressure. A tube humidifier (PDMSXA-1000, Perm Select) was placed before the PAC to maintain the gas humidity at a saturation level comparable to that of exhaled breath.

Sensor Performance Evaluation for CO_2 and O_2

The CO_2 gas concentration is ~0.04% in the atmosphere. However, the concentration of $ETCO_2$ in exhaled breath is much higher, approximately ranging from 4 to 5%. During a complete exhalation cycle, the range of CO_2 concentration variation is very wide, which poses a huge challenge to both the dynamic range and response time of the sensor. A standard CO_2/ synthetic air gas mixture was used for CO_2 gas detection evaluation. The optimal laser modulation amplitude that maximizes the second-harmonic signal is ~2.2 times the half-width at half-maximum (HWHM) of the Lorentzian-shaped absorption line.[50] As shown in Figure S6, the photoacoustic signal increases as the modulation amplitude rises. A modulation current depth of 22.5 mA was selected for the following experiment. Figure 3a shows the sensor response as a function of the CO_2 concentration varying from 0 to 1500 ppm CO_2/ synthetic air. A noise level of ~0.3 μV was measured for synthetic air. For a 300 ppm CO_2 synthetic air gas mixture, the detected signal resulted in 7.1 μV, which corresponds to a 1σ signal-to-noise ratio of ~70 and a noise equivalent concentration (NEC) of 12.6 ppm. The normalized noise equivalent absorption (NNEA) was calculated to be 2.9×10^{-8} $cm^{-1}\cdot W\cdot Hz^{-1/2}$, considering the employed detection bandwidth and optical power. To verify the linearity of the PAS-based sensor, the CO_2 signals measured at the different concentration values were averaged and are plotted in Figure 3b from 0 ppm to 1%. This plot with linear fitting R^2 values >0.99999 confirms the linearity of the sensor system response to the CO_2 concentration in a very wide range. A higher standard gas up to 8% was also tested, confirming the system's ability to discriminate and quantify CO_2 in breath gas mixtures.

The O_2 concentration in the atmosphere is ~21%, and it is continuously changing based on the atmospheric pressure, temperature, season, altitude, and forest coverage. During pulmonary gas exchange, oxygen diffuses from the alveoli into the blood, while carbon dioxide is released in the opposite direction, leading to a decrease in O_2 concentration in exhaled breath. As a result, the ETO_2 concentration typically ranges between 13 and 16%, depending on respiratory efficiency, metabolic activity, physical exercise, and pulmonary function. This physiological variability poses a challenge for high-precision O_2 sensing in breath analysis. As shown in Figure S7, the O_2 signal exhibits a linear growth with the increase of laser power under 20% O_2, without reaching saturation absorption, which is consistent with the deduction of eq S7. To achieve high detection sensitivity, an output power of 1.328 W was selected for the next experiment. Moreover, gas pressure is a critical parameter as it directly affects the *Q*-factor of the photoacoustic cell, the vibrational–translational (V-T) relaxation rate, and the intensity of its absorption spectrum. Figure S8 experimentally demonstrates a linear increase in the signal measured for 20% O_2 concentration with the gas pressure. Thereby, to maximize the signal and ensure an accurate measurement of exhaled gas concentration, a pressure controller was placed in front of the photoacoustic cell to maintain a constant and weak negative pressure of 720 Torr.

In order to evaluate the detection sensitivity of the sensor, 20% O_2/N_2 gas mixtures were diluted with pure N_2. A constant μV level background signal was observed under pure N_2 conditions. As depicted in Figure 3c, the photoacoustic signal maintains very small jitters in a constant standard gas under different concentrations. A $1\ \sigma$ detection limit of 18.4 ppm was obtained, which corresponds to an NNEA of 1.6×10^{-7} $cm^{-1}\cdot W\cdot Hz^{-1/2}$. The O_2 signals measured at the different concentration values were

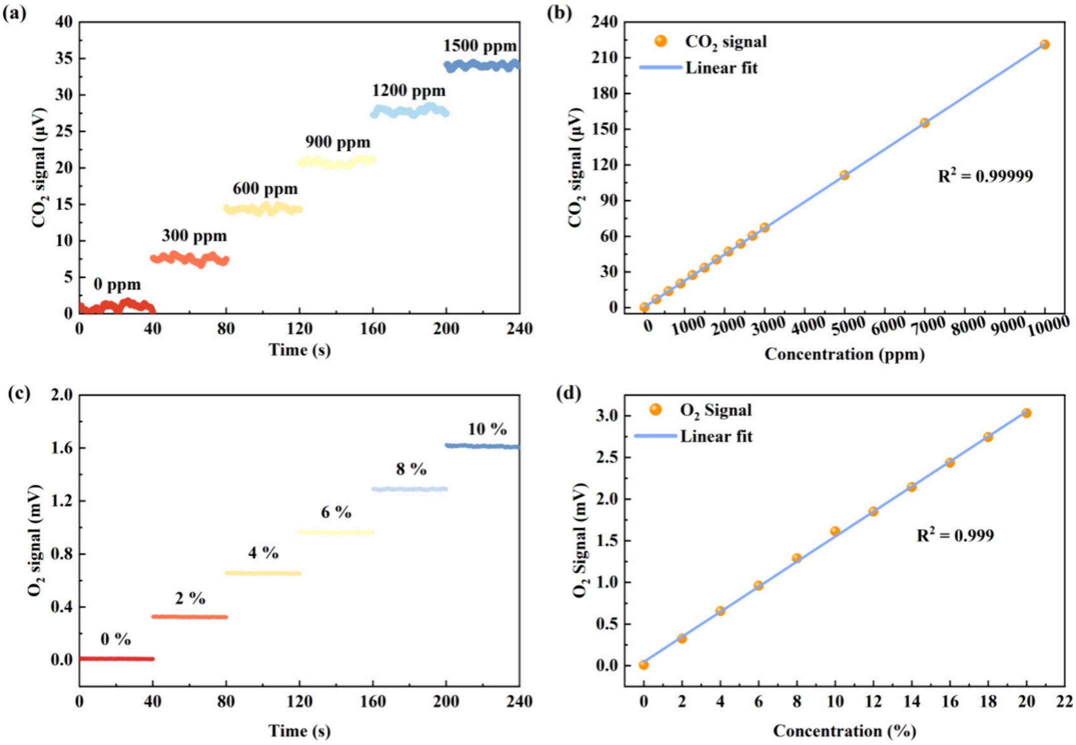

Figure 3. (a) CO_2 gas sensor toward 0–1500 ppm concentration steps. (b) Linear response from 0 to 1 % CO_2 gas. (c) O_2 gas sensor toward 0–10% concentration steps. (d) Linear response from 0 to 20 % O_2 gas.

averaged and are plotted in Figure 3d, and the linear fit gives an R^2 value of 0.999, confirming the sensor's linear response in all the investigated range.

SENSOR PERFORMANCE EVALUATION FOR ETCO$_2$ AND ETO$_2$

To evaluate the application value in medical monitoring and metabolic analysis, a healthy adult male weighing 60 kg and aged 24 was selected as the subject under test. To ensure the reliability of the experimental data, the subject refrained from consuming caffeine, alcohol, and other stimulants that may affect metabolism for 72 h prior to the experiment and avoided engaging in strenuous exercise. No food is consumed for 4 h before the experiment to eliminate interference from diet on exhaled gas composition. To prevent contamination of the photoacoustic cell and optical windows by particles originating from the oral cavity, a particle filter was installed upstream of the gas inlet. This measure effectively blocked particulate matter in the exhaled breath and ensured clean gas delivery into the photoacoustic cell. Figure 4 depicts the concentration changes of O_2 and CO_2 during a complete and slow respiratory cycle. The total data acquisition period was ~52 s, corresponding to the complete exhalation cycle. To better illustrate the temporal variations in CO_2 and O_2 concentrations during the respiratory cycle, a side-stream sampling method combined with prolonged exhalation was employed. The subject took a deep breath with an exhalation period greater than 5 s, and the exhaled gas was drawn into the sensor using a pump, resulting in clearer data profiles. The results indicate that during the inspiratory phase, the gas composition inside the detection device is highly consistent with ambient air, with an O_2 concentration of approximately 20.8% and a CO_2 concentration of ~400 ppm. As the breathing process proceeds, gas from the respiratory dead space mixes with alveolar gas, leading to a gradual transition of the gas composition from ambient air to metabolic products. In this mixing phase, the O_2 concentration gradually decreases, while the CO_2 concentration increases. In the alveolar gas phase, the exhaled air reflects the ongoing alveolar gas exchange, where O_2 diffuses into the blood and CO_2 diffuses from the blood into the alveolar space. This results in the characteristic end-tidal pattern, with CO_2 slowly increasing and O_2 slowly decreasing toward their final concentrations.[21,51−56] This behavior is consistent with established respiratory physiology, confirming that the developed gas detection system accurately captures the dynamic variations of O_2 and CO_2 during breathing.

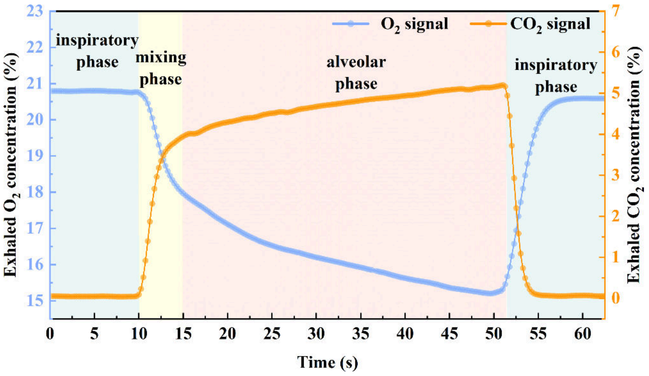

Figure 4. Detailed view of one breath cycle: inspiratory phase, mixing phase, and alveolar phase.

To further analyze the impact of respiratory frequency on the concentrations of O_2 and CO_2 in exhaled breath, two controlled

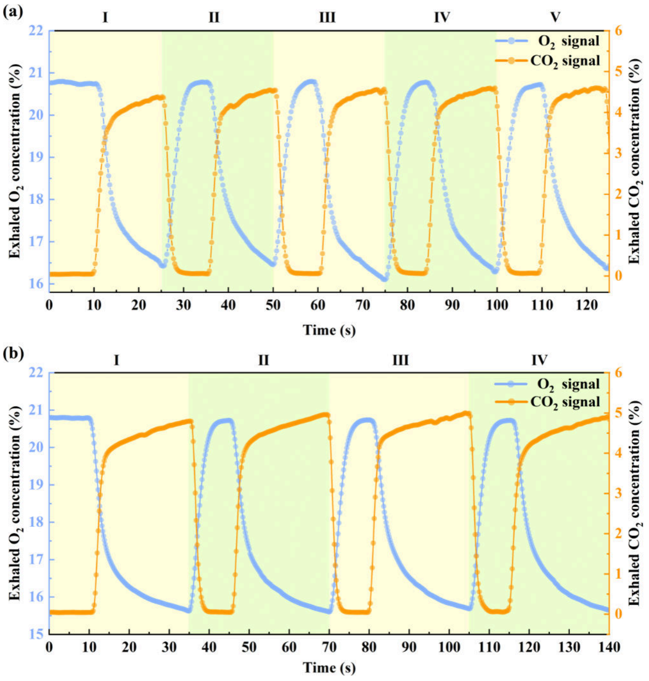

Figure 5. Exhaled O_2 and CO_2 concentrations during a respiratory cycle: (a) 10 s inhalation and 15 s exhalation; (b) 10 s inhalation and 25 s exhalation.

breathing patterns were tested: 10 s inhalation, followed by 15 s exhalation, and 10 s inhalation, followed by 25 s exhalation. Experimental data revealed that under slower breathing frequencies, the exhaled O_2 concentration decreased by approximately 3.1% overall, while the CO_2 concentration increased by approximately 8.7% compared to faster breathing. Figure 5a shows the O_2 and CO_2 concentration variations obtained for a 10 s inhalation and 15 s exhalation cycle, whereas Figure 5b illustrates the results for a 10 s inhalation and 25 s exhalation cycle. This trend indicates that a reduced respiratory frequency allows for a longer alveolar residence time of air, promoting more complete gas exchange between alveolar air and pulmonary capillary blood. Consequently, exhaled gas composition more accurately reflects the subject's metabolic state. These experimental results not only validate the reliability of the gas detection system developed in this study for real-time, high-precision monitoring of respiratory gases but also provide quantifiable experimental evidence supporting its potential applications in clinical respiratory assessment and metabolic analysis.

■ CONCLUSIONS

A compact differential photoacoustic cell was developed for real-time monitoring of exhaled CO_2 and O_2. Two resonant frequencies of 4110 and 13,115 Hz were employed for end-tidal CO_2 and O_2 detection. A red diode laser at 764.9 nm and a near-infrared DFB laser at 2004 nm served as excitation sources, achieving minimum detection limits of 12.6 ppm for CO_2 and 18.4 ppm for O_2. The corresponding NNEA values were 2.9×10^{-8} $\mathrm{cm^{-1}\cdot W\cdot Hz^{-1/2}}$ for CO_2 and 1.6×10^{-7} $\mathrm{cm^{-1}\cdot W\cdot Hz^{-one\text{-}half}}$ for O_2. The small gas cell volume enabled a fast response time (<0.5 s), allowing rapid tracking of concentration changes during exhalation. Breath tests conducted on a healthy subject showed that the O_2 concentration decreased, while the CO_2 concentration increased during exhalation, consistent with respiratory physiology. Variations in breathing frequencies produced distinct O_2 and CO_2 dynamics, confirming the reliability and responsiveness of the system.

The results indicate that the proposed PAS-based sensor enables accurate, sensitive, and dynamic monitoring of respiratory gases. The system offers key advantages of low cost, high sensitivity, and rapid response, making it highly promising for noninvasive clinical diagnosis, perioperative monitoring, and critical care applications. Moreover, with appropriate laser sources, the method can be further extended to detect additional exhaled biomarkers, significantly enhancing the scalability and forward-looking nature of the technology. For example, C_5H_{12} can indicate inflammatory diseases and transplant rejection; C_2H_6 reflects lipid peroxidation, oxidative stress, and lung cancer; $^{13}CO_2/^{12}CO_2$ can indicate Helicobacter pylori infection (peptic ulcers, gastric cancer); COS is associated with liver disease and acute rejection in lung transplant recipients; CS_2 is relevant for disulfiram treatment for alcoholism; NH_3 can indicate liver and renal diseases and exercise physiology; CH_2O can be a marker for cancerous tumors; CO reflects smoking response, lipid peroxidation, CO poisoning, and vascular smooth muscle response; C_3H_6O is indicative of ketosis and diabetes mellitus. This demonstrates that the system has the potential to serve as a versatile and cost-effective optical platform for comprehensive breath analysis.

■ ASSOCIATED CONTENT

Supporting Information

The Supporting Information is available free of charge at https://pubs.acs.org/doi/10.1021/acssensors.5c03835.

> Absorption line selection diagrams for ETO_2 and $ETCO_2$ detection; CO_2 absorption spectra images; experimental data images for the photoacoustic cell resonant frequency response in the range of 2000−12,000 Hz, duty cycle optimization of the 765 nm laser, modulation current optimization of the 2004 nm laser, power optimization of the 765 nm laser, and pressure optimization; detailed description and theoretical derivation of the photoacoustic signal generation principle, including relevant equations (DOCX)

■ AUTHOR INFORMATION

Corresponding Authors

Shuangping Zhang − *Department of Thoracic Surgery, Shanxi Province Cancer Hospital, Shanxi Hospital Affiliated to Cancer Hospital, Chinese Academy of Medical Sciences, Affiliated Tumor Hospital of Shanxi Medical University, Taiyuan 030013, China;* Email: zsp5500@163.com

Vincenzo Spagnolo − *PolySense Lab—Dipartimento Interateneo di Fisica, University and Politecnico of Bari, Bari 70126, Italy;* orcid.org/0000-0002-4867-8166; Email: vincenzoluigi.spagnolo@poliba.it

Hongpeng Wu − *State Key Laboratory of Quantum Optics and Quantum Optics Devices, Institute of Laser Spectroscopy, Shanxi University, Taiyuan 030006, Shanxi, China;* orcid.org/0009-0001-3648-8664; Email: wuhp@sxu.edu.cn

Huailiang Xu − *School of Optoelectronic Engineering, Xidian University, Xi'an 710071, Shaanxi, China;* Email: xuhuailiang@xidian.edu.cn

Authors

Xukun Yin – *School of Optoelectronic Engineering, Xidian University, Xi'an 710071, Shaanxi, China;* orcid.org/0000-0003-4840-9529

Chenchen Zhu – *School of Optoelectronic Engineering, Xidian University, Xi'an 710071, Shaanxi, China*

Xiu Yang – *School of Optoelectronic Engineering, Xidian University, Xi'an 710071, Shaanxi, China*

Lei Liu – *School of Optoelectronic Engineering, Xidian University, Xi'an 710071, Shaanxi, China*

Dacheng Zhang – *School of Optoelectronic Engineering, Xidian University, Xi'an 710071, Shaanxi, China*

Kaijie Xu – *School of Information Mechanics and Sensing Engineering, Xidian University, Xi'an 710071, Shaanxi, China*

Hongzhi Wang – *Department of Thoracic Surgery, Shanxi Province Cancer Hospital, Shanxi Hospital Affiliated to Cancer Hospital, Chinese Academy of Medical Sciences, Affiliated Tumor Hospital of Shanxi Medical University, Taiyuan 030013, China*

Nicoletta Ardito – *PolySense Lab—Dipartimento Interateneo di Fisica, University and Politecnico of Bari, Bari 70126, Italy;* orcid.org/0009-0005-9275-4129

Pietro Patimisco – *PolySense Lab—Dipartimento Interateneo di Fisica, University and Politecnico of Bari, Bari 70126, Italy;* orcid.org/0000-0002-7822-2397

Angelo Sampaolo – *PolySense Lab—Dipartimento Interateneo di Fisica, University and Politecnico of Bari, Bari 70126, Italy;* orcid.org/0000-0003-3790-3767

Complete contact information is available at:
https://pubs.acs.org/doi/10.1021/acssensors.5c03835

Author Contributions

This manuscript was written through contributions of all authors. All authors have given approval to the final version of the manuscript.

Funding

This work was partially funded by the National Natural Science Foundation of China (62475204, 62475137, 62205257); Fundamental Research Funds for the Central Universities (ZYTS25240, ZYTS25283); and Hangzhou Science and Technology Development Project (202204T04). The authors from the PolySense Lab acknowledge funding from the Project PNC 0000001 D3-4-Health—Digital Driven Diagnostics, prognostics and therapeutics for sustainable Health care (CUP: B83C22006120001) and MUR—Dipartimenti di Eccellenza (2023–2027)—Quantum Sensing and Modeling for One-Health (QuaSiModO).

Notes

The authors declare no competing financial interest.

■ REFERENCES

(1) Bruderer, T.; Gaisl, T.; Gaugg, M. T.; Nowak, N.; Streckenbach, B.; Müller, S.; Moeller, A.; Kohler, M.; Zenobi, R. On-line analysis of exhaled breath: focus review. *Chem. Rev.* **2019**, *119* (19), 10803–10828.

(2) Amann, A.; Miekisch, W.; Schubert, J.; Buszewski, B.; Ligor, T.; Jezierski, T.; Pleil, J.; Risby, T. Analysis of exhaled breath for disease detection. *Ann. Rev. Anal. Chem.* **2014**, 7 (1), 455–482.

(3) Mao, X.; Tan, Y.; Ye, H.; Yuan, T.; Peng, Y.; Zheng, P. Photoacoustic spectroscopy-based breath analysis for SIBO. *ACS Sens.* **2023**, *8* (12), 4728–4736.

(4) Vr, N.; Mohapatra, A. K.; Kartha, V. B.; Chidangil, S. Multiwavelength photoacoustic breath analysis sensor for the diagnosis of lung diseases: COPD and asthma. *ACS Sens.* **2023**, *8* (11), 4111–4120.

(5) Li, B.; Feng, C.; Wu, H.; Jia, S.; Dong, L. Photoacoustic heterodyne breath sensor for real-time measurement of human exhaled carbon monoxide. *Photoacoustics* **2023**, *27*, No. 100388.

(6) Yang, X.; Li, B.; Geng, X.; Zhao, T.; Yu, Q.; Hou, J.; Zhang, D.; Liang, Y.; Xu, K.; Wu, H.; Yin, X. Ppb-level formaldehyde sensor utilizing a compact 3D-printed differential photoacoustic cell and a 320 nm UV Laser. *Photoacoustics* **2025**, No. 100780.

(7) Nidheesh, V. R.; Mohapatra, A. K.; Nayak, R.; Unnikrishnan, V. K.; Kartha, V. B.; Chidangil, S. Bimodal UV photoacoustic and fluorescence sensor for breath analysis. *Sens. Actuators B: Chem.* **2023**, *379*, No. 133242.

(8) Wham, C.; Morin, T.; Sauaia, A.; McIntyre, R.; Urban, S.; McVaney, K.; Cohen, M.; Cralley, A.; Moore, E. E.; Campion, E. M. Prehospital ETCO$_2$ is predictive of death in intubated and non-intubated patients. *Am. J. Surg.* **2023**, *226* (6), 886–890.

(9) Lindsey, S.; Moran, T. P.; Diehl, J.; Snitzer, J.; McKenzie, K. L.; Janjua, N.; Ackerman, J.; McLaughlin, A.; MacAskill, R.; Carroll, S. M. Assessment of Preoxygenation using Real-Time End-Tidal Oxygen Measurements Versus Single-Breath End-Tidal Oxygen Measurements in Healthy Volunteers. *JACEP Open* **2025**, *6* (2), No. 100079.

(10) Li, X.; Chang, P.; Zhang, W. Online monitoring of propofol concentrations in exhaled breath. *Heliyon* **2024**, *10* (24), No. e39704.

(11) Ray, B.; Sangavi, V.; Vishwakarma, S.; Parmar, S.; Datar, S. Breath analysis using quartz tuning forks for predicting blood glucose levels using artificial neural networks. *ACS Sens.* **2024**, *9* (10), 5468–5478.

(12) Pauling, L.; Robinson, A. B.; Teranishi, R.; Cary, P. Quantitative analysis of urine vapor and breath by gas-liquid partition chromatography. *Proc. Natl. Acad. Sci. U. S. A.* **1971**, *68* (10), 2374–2376.

(13) Smith, D.; Španěl, P.; Herbig, J.; Beauchamp, J. Mass spectrometry for real-time quantitative breath analysis. *J. Breath Res.* **2014**, *8* (2), No. 027101.

(14) Henderson, B.; Slingers, G.; Pedrotti, M.; Pugliese, G.; Malaskova, M.; Bryant, L.; Lomonaco, T.; Ghimenti, S.; Moreno, S.; Cordell, R.; Harren, F. J. The peppermint breath test benchmark for PTR-MS and SIFT-MS. *J. Breath Res.* **2021**, *15* (4), No. 046005.

(15) Tang, Z.; Yang, J.; Xu, X.; Zhang, K.; Wang, H.; Luo, X.; Fang, M.; Huan, T.; Li, X. Breath and Blood Metabolomics: A Comparative Study Using SESI-HRMS/MS and UHPLC-ESI-HRMS/MS. *Environ. Health* **2025**, *3*, 596.

(16) Van den Broek, J.; Guntner, A. T.; Pratsinis, S. E. Highly selective and rapid breath isoprene sensing enabled by activated alumina filter. *ACS Sens.* **2018**, *14* (3), 677–683.

(17) Guntner, A. T.; Sievi, N. A.; Theodore, S. J.; Gulich, T.; Kohler, M.; Pratsinis, S. E. Noninvasive body fat burn monitoring from exhaled acetone with Si-doped WO$_3$-sensing nanoparticles. *Anal. Chem.* **2017**, *89* (19), 10578–10584.

(18) Güntner, A. T.; Pineau, N. J.; Chie, D.; Krumeich, F.; Pratsinis, S. E. Selective sensing of isoprene by Ti-doped ZnO for breath diagnostics. *J. Mater. Chem. B* **2016**, *4* (32), 5358–5366.

(19) Obermeier, J.; Trefz, P.; Wex, K.; Sabel, B.; Schubert, J. K.; Miekisch, W. Electrochemical sensor system for breath analysis of aldehydes, CO and NO. *J. Breath Res.* **2015**, *9* (1), No. 016008.

(20) Tütüncü, E.; Nägele, M.; Becker, S.; Fischer, M.; Koeth, J.; Wolf, C.; Köstler, S.; Ribitsch, V.; Teuber, A.; Gröger, M.; Kress, S. Advanced photonic sensors based on interband cascade lasers for real-time mouse breath analysis. *ACS Sens.* **2018**, *3* (9), 1743–1749.

(21) Li, Z.; Jiang, D.; Zhang, M.; Li, J. Diode laser absorption spectroscopy for real-time detection of breath oxygen. *Infrared Phys. Technol.* **2023**, *133*, No. 104815.

(22) Li, K.; Wang, B.; Yuan, M.; Yang, Z.; Yu, C.; Zheng, W. CO detection system based on TDLAS using a 4.625 μm interband cascaded laser. *Int. J. Environ. Res. Public Health* **2022**, *19* (19), 12828.

(23) Sun, M.; Jiang, C.; Gong, Z.; Zhao, X.; Chen, Z.; Wang, Z.; Kang, M.; Li, Y.; Wang, C. A fully integrated standalone portable cavity ringdown breath acetone analyzer. *Rev. Sci. Instrum.* **2015**, *86* (9), No. 095003.

(24) Van Mastrigt , E.; Reyes-Reyes, A.; Brand, K.; Bhattacharya, N.; Urbach, H. P.; Stubbs, A. P.; De Jongste , J. C.; Pijnenburg, M. W. Exhaled breath profiling using broadband quantum cascade laser-based spectroscopy in healthy children and children with asthma and cystic fibrosis. *J. Breath Res.* **2016**, *10* (2), No. 026003.

(25) Yin, X.; Wu, H.; Dong, L.; Li, B.; Ma, W.; Zhang, L.; Yin, W.; Biao, L.; Jia, S.; Tittel, F. K. Ppb-level SO_2 photoacoustic sensors with a suppressed absorption−desorption effect by using a 7.41 μm external-cavity quantum cascade laser. *ACS Sens.* **2020**, *5* (2), 549−556.

(26) Sang, C.; Zhang, C.; Wang, R.; Qiao, S.; He, Y.; Ma, Y. Tapered acoustic resonator-based quartz-enhanced photoacoustic spectroscopy. *Opt. Lett.* **2025**, *50* (15), 4646−4649.

(27) Kinjalk, K.; Paciolla, F.; Sun, B.; Zifarelli, A.; Menduni, G.; Giglio, M.; Wu, H.; Dong, L.; Ayache, D.; Pinto, D.; Vicet, A. Highly selective and sensitive detection of volatile organic compounds using long wavelength InAs-based quantum cascade lasers through quartz-enhanced photoacoustic spectroscopy. *Appl. Phys. Rev.* **2024**, *11* (2), No. 021427.

(28) Wang, L.; Lv, H.; Zhao, Y.; Wang, C.; Luo, H.; Lin, H.; Xie, J.; Zhu, W.; Zhong, Y.; Liu, B.; Yu, J. Sub-ppb level HCN photoacoustic sensor employing dual-tube resonator enhanced clamp-type tuning fork and U-net neural network noise filter. *Photoacoustics* **2024**, *38*, No. 100629.

(29) Li, C.; Han, X.; Guo, M.; Qi, H.; Zhang, J.; Zhao, X.; Chen, K. Cantilever-enhanced fiber-optic photoacoustic spectrophone for low-pressure gas detection. *Anal. Chem.* **2025**, *97* (1), 838−847.

(30) Yin, X.; Dong, L.; Wu, H.; Zheng, H.; Ma, W.; Zhang, L.; Yin, W.; Jia, S.; Tittel, F. K. Sub-ppb nitrogen dioxide detection with a large linear dynamic range by use of a differential photoacoustic cell and a 3.5 W blue multimode diode laser. *Sens. Actuators B: Chem.* **2017**, *247*, 329−335.

(31) Wang, Z.; Nie, Q.; Sun, H.; Wang, Q.; Borri, S.; De Natale, P.; Ren, W. Cavity-enhanced photoacoustic dual-comb spectroscopy. *Light: Sci. Appl.* **2024**, *13* (1), 11.

(32) Yin, X.; Wu, H.; Dong, L.; Ma, W.; Zhang, L.; Yin, W.; Biao, L.; Jia, S.; Tittel, F. K. Ppb-level photoacoustic sensor system for saturation-free CO detection of SF_6 decomposition by use of a 10 W fiber-amplified near-infrared diode laser. *Sens. Actuators B: Chem.* **2019**, *282*, 567−573.

(33) Duan, L.; Guan, Z.; Yuan, Z.; Xie, L.; Zheng, Z.; Ye, W.; Zheng, C. Photoacoustic Ringdown Spectroscopy for Rapid Hydrogen Detection. *Anal. Chem.* **2025**, *97*, 12845.

(34) Yin, X.; Dong, L.; Wu, H.; Gao, M.; Zhang, L.; Zhang, X.; Liu, L.; Shao, X.; Tittel, F. K. Compact QEPAS humidity sensor in SF_6 buffer gas for high-voltage gas power systems. *Photoacoustics* **2022**, *25*, No. 100319.

(35) Li, J.; Deng, H.; Sun, J.; Yu, B.; Fischer, H. Simultaneous atmospheric CO, N_2O and H_2O detection using a single quantum cascade laser sensor based on dual-spectroscopy techniques. *Sens. Actuators B: Chem.* **2016**, *231*, 723−732.

(36) Liu, N.; Xu, L.; Li, J. Self-calibrated wavelength modulation spectroscopy based on 2 f/1 f amplitude and integral area for trace gas sensing. *Opt. Quant. Electron.* **2023**, *55* (1), 22.

(37) Xu, L.; Zhou, S.; Liu, N.; Zhang, M.; Liang, J.; Li, J. Multigas sensing technique based on quartz crystal tuning fork-enhanced laser spectroscopy. *Anal. Chem.* **2020**, *92* (20), 14153−14163.

(38) Huang, Q.; Wei, Y.; Li, J. Simultaneous detection of multiple gases using multi-resonance photoacoustic spectroscopy. *Sens. Actuators B: Chem.* **2022**, *369*, No. 132234.

(39) Qiao, S.; He, Y.; Sun, H.; Patimisco, P.; Sampaolo, A.; Spagnolo, V.; Ma, Y. Ultra-highly sensitive dual gases detection based on photoacoustic spectroscopy by exploiting a long-wave, high-power, wide-tunable, single-longitudinal-mode solid-state laser. *Light: Sci. Appl.* **2024**, *13* (1), 100.

(40) Wei, Q.; Li, B.; Zhao, B.; Wang, Y. Highly Sensitive Photoacoustic Multi-Gas Detection of SF_6 Decomposition Components. *Photonic Sens.* **2025**, *15* (4), No. 250430.

(41) Wang, Q.; Wang, Z.; Zhang, H.; Jiang, S.; Wang, Y.; Jin, W.; Ren, W. Dual-comb photothermal spectroscopy. *Nat. Commun.* **2022**, *13* (1), 2181.

(42) Gordon, I. E.; Rothman, L. S.; Hargreaves, E. R.; Hashemi, R.; Karlovets, E. V.; Skinner, F. M.; Conway, E. K.; Hill, C.; Kochanov, R. V.; Tan, Y.; Wcisło, P. The HITRAN2020 molecular spectroscopic database. *J. Quant. Spectrosc. Radiat. Transf.* **2022**, *277*, No. 107949.

(43) Xiong, S.; Yin, X.; Wang, Q.; Xia, J.; Chen, Z.; Lei, H.; Yan, X.; Zhu, A.; Qiu, F.; Chen, B.; Wang, Q. Photoacoustic spectroscopy gas detection technology research progress. *Appl. Spectrosc.* **2024**, *78* (2), 139−158.

(44) Fathy, A.; Sabry, Y. M.; Hunter, I. W.; Khalil, D.; Bourouina, T. Direct absorption and photoacoustic spectroscopy for gas sensing and analysis: a critical review. *Laser Photonics Rev.* **2022**, *16* (8), No. 2100556.

(45) Dumitras, D. C.; Dutu, D. C.; Matei, C.; Magureanu, A. M.; Petrus, M.; Popa, C. Laser photoacoustic spectroscopy: principles, instrumentation, and characterization. *J. Optoelectron. Adv. Mater.* **2007**, *9* (12), 3655.

(46) Fu, L.; Lu, P.; Pan, Y.; Zhong, Y.; Sima, C.; Wu, Q.; Zhang, J.; Cui, L.; Liu, D. All-optical non-resonant photoacoustic spectroscopy for multicomponent gas detection based on aseismic photoacoustic cell. *Photoacoustics* **2023**, *34*, No. 100571.

(47) Wang, W.; Zhang, T.; Zhang, Q.; Wei, Y.; Wang, L.; Gu, Y.; Li, C. Photoacoustic spectroscopy sensor based on a dual-resonance photoacoustic cell for simultaneous detection of two-component gases. *Infrared Phys. Technol.* **2025**, *150*, No. 106047.

(48) Zhang, C.; Gao, Y.; Cui, R.; Zhang, H.; Tian, J.; Tang, Y.; Yang, L.; Feng, C.; Patimisco, P.; Sampaolo, A.; Spagnolo, V. Enhancing photoacoustic trace gas detection via a CNN−transformer denoising framework. *Photoacoustics* **2025**, *45*, No. 100758.

(49) Wang, F.; Wu, J.; Cheng, Y.; Fu, L.; Zhang, J.; Wang, Q. Simultaneous detection of greenhouse gases CH_4 and CO_2 based on a dual differential photoacoustic spectroscopy system. *Opt. Express* **2023**, *31* (21), 33898−33913.

(50) Yin, X.; Dong, L.; Zheng, H.; Liu, X.; Wu, H.; Yang, Y.; Ma, W.; Zhang, L.; Yin, W.; Biao, L.; Jia, S. Impact of humidity on quartz-enhanced photoacoustic spectroscopy based CO detection using a near-IR telecommunication diode laser. *Sensors* **2016**, *16* (2), 162.

(51) Miekisch, W.; Kischkel, S.; Sawacki, A.; Liebau, T.; Mieth, M.; Schubert, J. K. Impact of sampling procedures on the results of breath analysis. *J. Breath Res.* **2008**, *2* (2), No. 026007.

(52) Lawal, O.; Ahmed, W. M.; Nijsen, T. M.; Goodacre, R.; Fowler, S. J. Exhaled breath analysis: a review of 'breath-taking'methods for off-line analysis. *Metabolomics* **2017**, *13* (10), 110.

(53) Kolle, C.; Gruber, W.; Trettnak, W.; Biebernik, K.; Dolezal, C.; Reininger, F.; O'Leary, P. Fast optochemical sensor for continuous monitoring of oxygen in breath-gas analysis. *Sens. Actuators B: Chem.* **1997**, *38* (1-3), 141−149.

(54) Cummings, B.; Hamilton, M. L.; Ciaffoni, L.; Pragnell, T. R.; Peverall, R.; Ritchie, G. A.; Hancock, G.; Robbins, P. A. Laser-based absorption spectroscopy as a technique for rapid in-line analysis of respired gas concentrations of O_2 and CO_2. *J. Appl. Physiol.* **2011**, *111* (1), 303−307.

(55) Yin, X.; Hu, Q.; Yang, X.; Xu, K.; Liang, Y.; Hou, J.; Sampaolo, A.; Patimisco, P.; Spagnolo, V.; Zhang, D.; Liu, Z.; Xu, H.; Wu, H. Ppb-level HF sensor in GeF_4 gas matrices with a 76 m TDLAS cell. *Sens. Actuators B: Chem.* **2025**, *449* (15), No. 139141.

(56) Burke, C.S.; Moore, J.P.; Wencel, D.; Maccraith, B.D. Development of a compact optical sensor for real-time, breath-by-breath detection of oxygen. *J. Breath Res.* **2008**, *2* (3), No. 037012.